NANO LETTERS

Letter

pubs.acs.org/NanoLett

Real-Time Atomic Force Microscopy Imaging of Block Copolymer Directed Self Assembly

Jonathan Raybin,[†] Jiaxing Ren,[‡] Xuanxuan Chen,[‡] Roel Gronheid,[§] Paul F. Nealey,[‡] and S. J. Sibener*[,†]

[†]The James Franck Institute and Department of Chemistry, The University of Chicago, 929 East 57th Street, Chicago, Illinois 60637, United States

[‡]The Institute for Molecular Engineering, The University of Chicago, 5640 South Ellis Avenue, Chicago, Illinois 60637, United States

[§]IMEC Kapeldreef 75, B-3001 Leuven, Belgium

Supporting Information

ABSTRACT: The kinetics of directed self-assembly of symmetric PS-*b*-PMMA diblock copolymer on chemically patterned templates were measured during in situ thermal annealing. Although these chemical guide patterns lead to well-aligned, defect-free lamellar patterns at thermodynamic equilibrium, in practice, challenges remain in understanding and optimizing the kinetic evolution for technological applications. High-speed, environmentally controlled atomic force microscopy imaging was used to track pattern evolution on the time scale of individual microdomain connections in real space and time, allowing the direct visualization of defect healing mechanisms. When we apply this highly general technique to films on chemically patterned substrates, we find that pattern alignment is mediated by a metastable nonbulk morphology unique to these samples, referred to as the "stitch" morphology. We observe diverse and anisotropic mechanisms for the conversion from this morphology to equilibrium lamellar stripes. Directed self-assembly on chemical templates is observed to follow exponential kinetics with an apparent energetic barrier of 360 ± 80 kJ/mol from 210−230 °C, a significant enhancement when compared with ordering rates on unpatterned substrates. Ultimately, from local imaging, we find that the presence of a chemical guiding field causes morphological ordering and lamellar alignment to occur irreversibly.

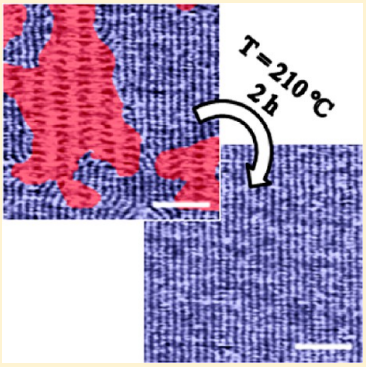

KEYWORDS: *Chemoepitaxy, chemical templates, environmental AFM, PS-b-PMMA*

The self-assembled, nanoscale patterns of block copolymers (BCP) have long been viewed as an attractive platform for fabricating semiconductor devices.[1−4] Nanoscopic control over polymer morphology is necessary to achieve the levels of registration and perfection required for such processes, and a variety of strategies have been developed for this purpose. Generally, these techniques break the in-plane symmetry of BCP films through the application of external long-range fields (such as shear flow[5] or electric fields)[6,7] or locally through substrate modification to enforce a single preferred orientation.

Directed self-assembly (DSA) methods, which use lithographically defined templates with chemical contrast (chemoepitaxy)[8,9] or topographical features (graphoepitaxy),[10] enforce a single preferred orientation and have been demonstrated to yield large-scale single-crystalline microphases with lower defect densities than long-range alignment strategies.[11,12] DSA patterns may achieve smaller features than their lithographic templates through pattern multiplication.[9]

For DSA to be successfully implemented in high-volume semiconductor manufacturing, defect annihilation kinetics must be able to achieve defect levels of 0.01/cm^2 within process-friendly time scales. Molecular simulations have predicted that the defects are not thermodynamically favorable but rather represent nonequilibrium structures that are kinetically trapped.[13−15] In the polymer system studied here, a simple dislocation defect has a free energy excess of $\Delta F \sim 100\ k_B T$ over the aligned structure and is highly unfavorable. This large thermodynamic excess is derived from the collective strain of the many individual polymer chains participating in the defect.[16] The annihilation of even simple, single-domain defects involves the formation of a series of transition states that constitute an uphill thermodynamic barrier. For more-complex defects that involve multiple domains, the thermodynamic landscape becomes increasingly complicated, and intermediate structures are more likely to remain trapped in a defective state. To understand the formation and annihilation of defects, in this work, we probe the evolution of BCP structures on DSA chemical patterns during thermal annealing through in situ high-speed AFM imaging.

Many studies have investigated the kinetics of annealing of block copolymer thin films. Grazing-incidence small-angle X-ray scattering (GI-SAXS) experiments have observed microphase separation and phase transitions during solvent vapor annealing.[17,18] Still, GI-SAXS scattering patterns reflect global morphological changes and cannot distinguish local defect

Received: September 10, 2017
Revised: November 9, 2017
Published: November 27, 2017

DOI: 10.1021/acs.nanolett.7b03881
Nano Lett. 2017, 17, 7717−7723

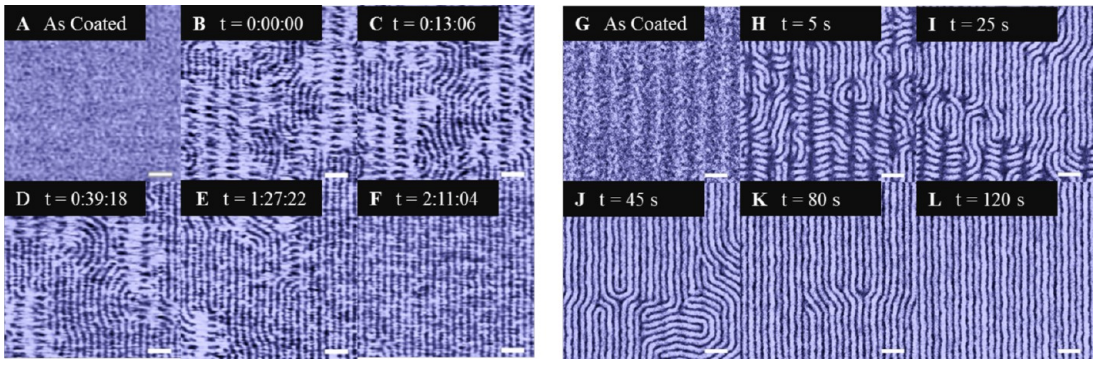

Figure 1. (a–f) AFM time-series phase images of lamella-forming PS-*b*-PMMA films on a chemical guide pattern as cast (a) and captured throughout in situ thermal annealing at 210 °C (b–f). Dark domains correspond to PMMA, and light domains correspond to PS. These frames are representative of a continuous movie included as Supporting Information. (g–l) SEM images showing a series of lamella-forming PS-*b*-PMMA samples as cast (g) and following discrete thermal annealing intervals at 250 °C (h–l). The contrast is inverted in SEM images; dark domains correspond to PS, and light domains correspond to PMMA. Scale bars are 100 nm.

structures. Ex situ imaging methods have examined pattern development following arrested annealing intervals, revealing a $t^{1/4}$ power law for the growth aligned grains with annealing rates sensitive to polymer morphology.[19−22] In situ AFM has been used to trace the kinetics of BCP healing,[23] defect annihilation mechanisms and rates within topographic channels,[24−26] and grain-coarsening behavior.[24] However, previous in situ AFM imaging experiments have been limited by slower scan rates and lacked sufficient time resolution to map the dynamics of pattern evolution on the time scale of individual domain linkages and disconnections. Here, we track polymer evolution in real time and space to elucidate specific defect annealing mechanisms.

We have used environmentally controlled in situ AFM to continuously trace the evolution of polymer structure during thermal annealing in real time; see Figure 1a–f. These AFM micrographs reveal the progression of the polymer morphology toward alignment, in which we observe three distinct and hierarchical processes: (1) microphase separation, (2) morphological stitched-to-perpendicular lamellar ordering, and (3) lamellar alignment. Microphase separation of the PS and PMMA blocks occurs rapidly before we began imaging at 210 °C. (Thermal drift prevents stable imaging during the initial temperature ramp.) Initially, following the microphase separation, the polymer has not yet fully adopted the perpendicular lamellar morphology, as seen in Figure 2a. Instead, images show the coexistence of a second morphological phase, termed the "stitch" morphology (Figure 2b), characterized by short PMMA stitches in a PS matrix to the chemical guide pattern, alongside the perpendicular lamellar

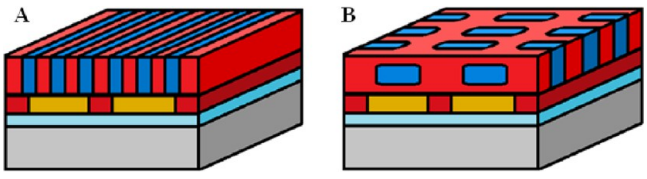

Figure 2. Schematic cross-sections of the thin-film morphology. (a) Schematic of the lamellar morphology with epitaxial alignment to the underlying PS guide stripes. (b) Schematic of the metastable "stitch" morphology, a superstructure of lamella parallel and perpendicular to the substrate that is commensurate with the DSA pattern. Key: red, PS domains; blue, PMMA domains; dark red, PS guide stripes; yellow = random polymer brush; light blue, native oxide; gray, silicon substrate.

morphology. Although AFM images reveal only two-dimensional surface patterns, we have characterized the three-dimensional structure using scanning electron microscope (SEM) tomography, experiments that will be discussed in a forthcoming publication. The stitch morphology forms a regular pattern including columns of orthogonal stitches spaced by columns of lamella oriented parallel to the substrate. As illustrated in Figure 2b, parallel lamellae reside above the brush regions of the guide pattern, and half layers of PS coat both the substrate and atmospheric interfaces. The stitch morphology is not a bulk equilibrium block copolymer phase; it is a metastable superstructure of perpendicular and parallel lamella unique to thin films on chemically patterned substrates.

The stitch morphology has not been studied theoretically, and its precise energetics have not yet been characterized. We propose several mechanisms that can contribute to the orthogonally aligned, metastable structure. First, orthogonal alignment may be favored to reduce frustration due to mismatch between the relative periodicities of the guide pattern and the epitaxial film.[8] Second, alignment may be influenced by the topography of the chemical template. In the guide pattern, the guide stripes are ∼5 nm thicker than the brush regions producing a corrugated surface.[27] Lamellar domains have been shown to orient perpendicular to surface corrugation to reduce stretching and compression of polymer chains along their long axis.[28]

As annealing continues, perpendicular lamellar grains coarsen and stitched grains shrink. Concurrently, defects including dislocations and disclinations in the lamellar grains annihilate, yielding a well-aligned film after roughly 135 min of annealing at 210 °C. The final equilibrium patterns have a pitch of 28 nm, consistent with 3-fold pattern multiplication on the 84 nm templates.

The perpendicular lamella and stitch phases may be easily distinguished in AFM images due to their distinct surface patterns. PS composes a larger fraction of the atmospheric interface for the stitch morphology, $f_{PS,stitch}$ = 72%, than for the perpendicular lamellar phase, $f_{PS,\perp lam}$ = 47%, which suggests the formation of parallel lamella with PS at the top surface. Note that surfaces of randomly oriented lamella have comparable PS coverage to aligned lamella despite their high defect densities. Although the Flory–Huggins interaction parameters of PS and PMMA with air are very similar at the annealing temperatures, the atmospheric interface has a slight PS preference at 200 °C,

DOI: 10.1021/acs.nanolett.7b03881
Nano Lett. 2017, 17, 7717−7723

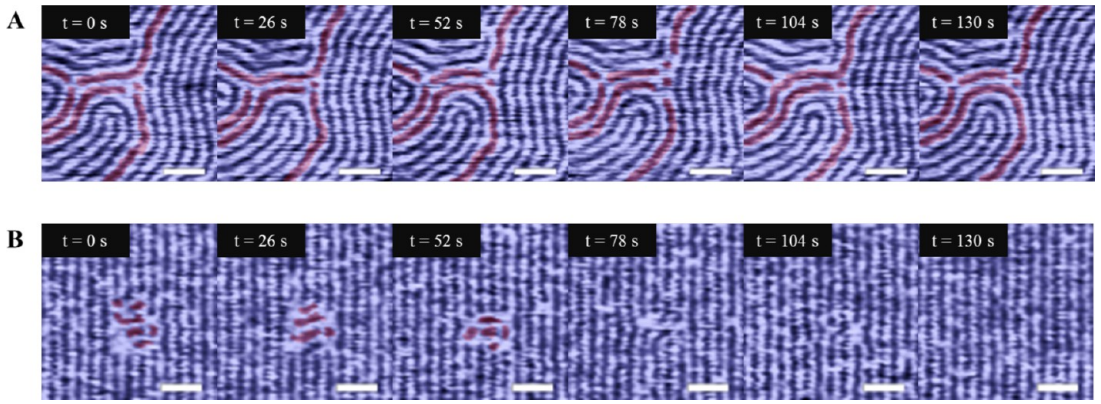

Figure 3. Time sequence at 26 s intervals of AFM images of lamella-forming PS-*b*-PMMA on a random brush substrate (a) during in situ thermal annealing at 210 °C, showing disconnections and reconnections of strained junctions. Red highlights are included for clarity. A time sequence of symmetric PS-*b*-PMMA on a chemically patterned substrate (b) under identical annealing conditions shows the conversion of a short stitched domain, highlighted in red, to aligned perpendicular lamella. Scale bars are 100 nm.

as observed by Mansky et al., which we postulate may play a role in stabilizing the stitch morphology.[29] However, this preference disappeared at temperatures above 225 °C.

We repeated these thermal annealing experiments at 250 °C to achieve industrially relevant conditions. However, pattern evolution progressed too quickly to be captured by in situ AFM imaging. Instead, we examined a series of samples with truncated annealing times and imaged the samples with scanning electron microscopy (Figure 1g–l). Under these conditions, a similar morphological progression was observed at faster time scales. Initial microphase separation occurred rapidly, within 5 s at 250 °C. We again observe the coexistence of stitched and perpendicular lamellar phases for annealing times under 25 s. Many in-plane lamellar defects persisted following the complete conversion of stitched grains, but continued thermal treatment yielded uniform perpendicular lamella and, ultimately, a well-aligned, low-defect structure within 2 min.

While SEM imaging confirms the overall progression of thermal annealing, these ex situ studies are necessarily discontinuous, and each measurement must probe a separate sample. High-speed in situ AFM complements SEM analysis by enabling direct monitoring of polymer morphologies in a single region in real time. Furthermore, AFM imaging is completely nondestructive, whereas electron beam exposure during SEM imaging causes sample damage including backbone fragmentation and cross-linking.

As a point of comparison, we also tracked the dynamics of lamellar films on unpatterned substrates, shown in Figure 3a. A random copolymer brush that is nonpreferential toward PS and PMMA ensured that the lamella would be oriented perpendicular to the interface.[30] In the absence of an external field, the pattern exhibits a polycrystalline grain structure with high defect density, a characteristic "fingerprint" pattern. As expected, no stitch phase was observed because the stitch morphology arises due to the influence of the chemically patterned template. Thermal annealing of fingerprint patterns under the conditions and time scales used for patterned substrates showed minimal grain growth or overall ordering.

During the thermal annealing of unpatterned substrates, we witnessed frequent microdomain disconnections and reconnections in regions along the boundaries of orientational grains. The lamellae at grain junctions, highlighted in red for clarity, experience conflicting alignment stresses from the neighboring grains. In this isotropic substrate environment, there is no strong thermodynamic preference toward a unique lamellar orientation and the polymer may adopt any morphology from an array of nearly degenerate states. During annealing, we observed polymer microdomains in these regions stochastically sample this selection of possible states. We note that domain evolution is reversible because the pattern frequently backtracks to previously explored states, slowing the development of larger, well-aligned grains. Within the 2 min time period depicted, only minimal changes to the overall connectivity have occurred and the grain sizes have not changed. In our experiments, AFM imaging may only probe lamellar connectivity at the surface. Previous tomographic analysis of these sites has shown similar variation in domain connectivity while suggesting a more-complex three-dimensional structure.[31]

In contrast, polymer films on patterned templates rapidly converge onto a single thermodynamic minimum state. Figure 3b follows the complete conversion and alignment of a short column of stitched domains. These frames depict a polymer sample at the same temperature and over the same time period as the unpatterned sample shown in Figure 3a. Similar microdomain disconnection and reconnection events occur, allowing the pattern to sample different connectivity states. In contrast to the unpatterned samples, however, along the boundaries of stitched grains neighboring aligned lamella and the underlying chemical pattern provide stable boundary conditions that direct alignment of the polymer and facilitate the elimination of defects. Only a single aligned lamellar orientation is thermodynamically favored. Strikingly, the strong thermodynamic gradient provided an irreversible path to alignment; we never observed aligned lamella reverting to misaligned or stitched domains. This result offers proof for earlier simulation predictions that DSA establishes a significantly lower free energy for the aligned state such that the alignment process is irreversible.[13] The irreversibility of defect removal is crucial for DSA to be able to achieve the low defect level required by advanced lithography applications.

The kinetics of conversion from the stitch morphology is fundamental to understanding the organization of films on chemical patterns. This process is of particular interest because it appears to limit the overall alignment rate of the film. While the stitched-to-perpendicular lamella conversion process initially yields films with a high defect density, most of these lamellar defects are resolved before the stitch morphology has

DOI: 10.1021/acs.nanolett.7b03881
Nano Lett. 2017, 17, 7717–7723

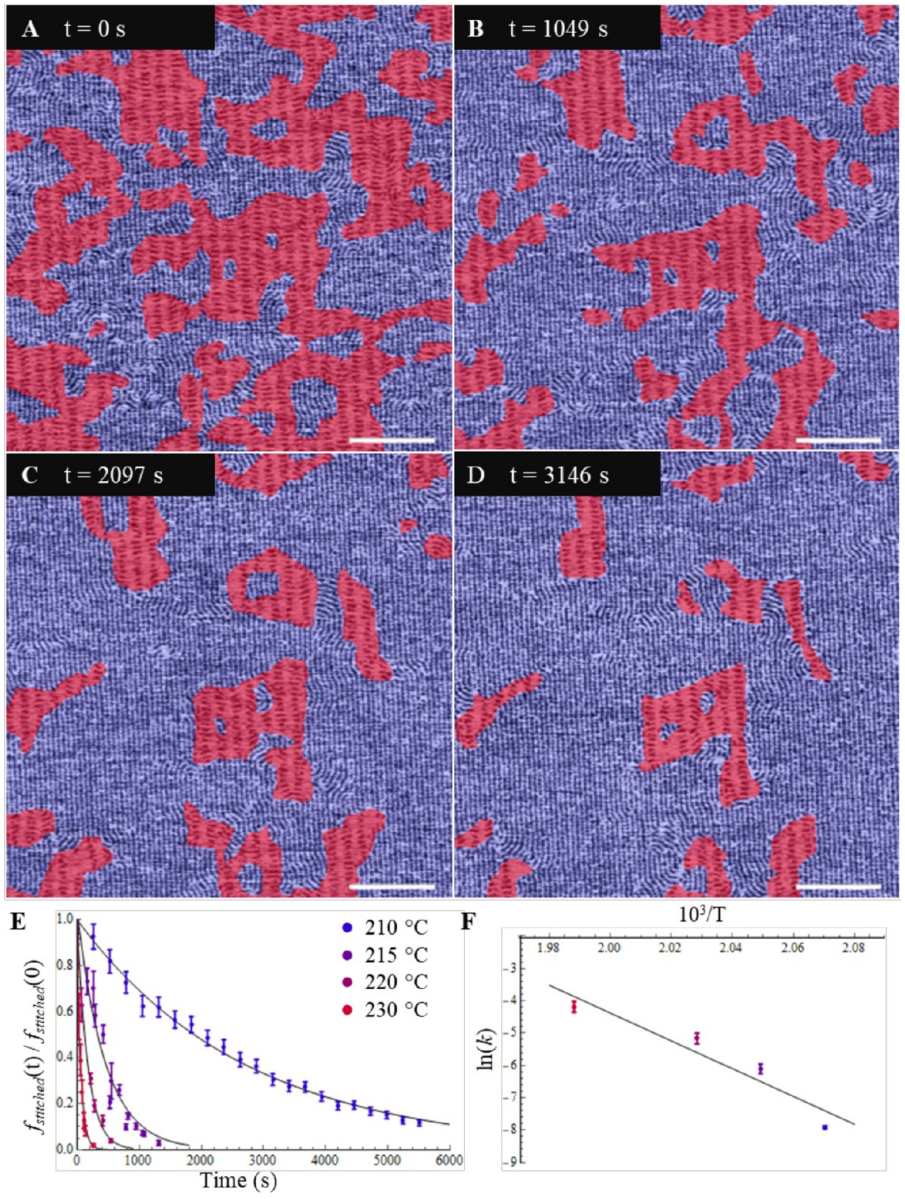

Figure 4. AFM images (a–d) of the PS-*b*-PMMA during i thermal annealing at 210 °C analyzed for kinetic data. The stitched domains have been highlighted in red. Scale bars are 500 nm. The area fraction of the stitched domains plotted over time (e) for several temperatures and fit by single exponentials curves. AFM movie data showing annealing at 210 and 230 °C are including in the Supporting Information. Also shown is an Arrhenius plot (f) yielding an apparent energetic barrier of 360 ± 80 kJ/mol at experimental temperatures.

fully converted. In this manner, the energetics of the stitch phase mediates the overall alignment.

We therefore examined the kinetics of this morphological transition more closely. In our initial images at 210 °C, the metastable stitched domains cover a majority of the surface. Over time, the area of the stitched regions (marked in red in Figure 4a–d) decreases, reducing its surface coverage and leaving disconnected grains. The surface coverage of the stitch morphology is plotted over time in Figure 4e. Each experimental data set represents a continuous time series of AFM images, and each data point corresponds to a single image. Our data for 220 °C are drawn from two separate experiments, demonstrating the reproducibility of these measurements. annealing at 210 °C, surface coverage data could be closely fit to a single exponential decay with time constant τ = 2440 s:

$$\frac{f_{\text{stitch}}(t - t_0)}{f_{\text{stitch}}(t_0)} = e^{-(t-t_0)/\tau}$$

This exponential dependence represents a significant rate enhancement over the $t^{1/4}$ power laws governing the grain growth of unpatterned films.[18] The normalized expression fits our data independently of initial surface coverage of the stitch phase. We repeated these measurements over a series of temperatures, finding thermally activated kinetics. Fitting our data to an Arrhenius plot finds an apparent energetic barrier of E_a = 360 ± 80 kJ/mol from 210–230 °C (corresponding to roughly 80 ± 20 k_BT at experimental temperatures). However, we must qualify this measurement by noting that defect annealing does not follow a singular topological mechanism and cannot be described by a unique potential energy surface. Indeed, the apparent curvature of our Arrhenius plot suggests a

DOI: 10.1021/acs.nanolett.7b03881
Nano Lett. 2017, 17, 7717–7723

potentially more-complex temperature dependence. As such, the measured value reflects only an average effective barrier for the chain reorientation of PS and PMMA domains into forming perpendicular lamellae, the microscopic process common to each of these mechanisms.

Simulations by Hur et al. have predicted reaction coordinates for defect annihilation of single dislocation pairs on chemically patterned templates. Their observed annihilation pathway includes multiple transition states and has an overall kinetic barrier roughly 15 k_BT for nonadjacent dislocation dipoles.[13] Per our observations, conversion from the stitch morphology involves a larger activation energy than resolving in-plane lamellar defects. For comparison, previous studies of grain growth for lamellar PS-*b*-PMMA with 32.3 kg/mol molecular weight have found barriers of E_a = 900 kJ/mol (roughly 230 k_BT) from 180−220 °C on unpatterned silicon substrates.[21]

As noted above, alignment requires the subsequent reorganization and annihilation of defects in the resulting lamellar microstructure. The high defect density of these films during the early stages of thermal annealing provides ample opportunities to study the annihilation of different defect structures. In most cases lamellar defects reorganized more quickly than the stitched-to-perpendicular lamellar conversion, but longer-lived structures occasionally formed depending on the local defect environment. Notably we observed differences in the resulting lamellar conformation dependent on the direction of grain growth during the stitched-to-perpendicular lamellar conversion.

When stitches were converted to lamella orthogonal to the direction of the guide stripe, as shown in Figure 5a, grain growth proceeded by one stitched column at a time (corresponding to one guide pattern period). First, stitches adjacent to the grain boundary rotate to form aligned lamellar segments. The short new lamellae then extend upward and downward to produce an entire aligned column. When the lamella meet other aligned regions, the new stripes then directly connect to form continuous aligned domains without the formation of intermediate defect states. After the complete conversion of one stitched column, the end state is self-similar to the starting conditions, and the process may be repeated. In particular, we note that this grain growth mechanism provided a direct path to lamella with robust alignment, bypassing the late-stage lamellar alignment processes.

However, in other cases, stitched columns may connect with each other rather than with neighboring lamellar domains, as shown in Figure 5b. This process leads to grain growth parallel to the direction of the guide stripe. The stitched columns connect to form lamellar segments orthogonal to the underlying guide pattern. When aligned lamellae connect with misoriented segments, they yield curved domains that ultimately form disclinations, an example of which is shown at the end of the time series in Figure 5b. Disclinations were stabilized by the neighboring stitched morphology and were generally observed to persist as longer-lived structures at 210 °C following the complete stitched-to-perpendicular lamella conversion. Although we witnessed many examples of the two cases pictured in Figure 5, in practice, the conversion process is highly dependent on the local defect structure and often follows a combination of the mechanisms described here.

Misregistration of the lamellar stripes within domains also yields single dislocation defects, as highlighted in Figure 6a. Lamellar misregistry extends across multiple domains connecting spatially separated defect sites. Dislocations are attracted to

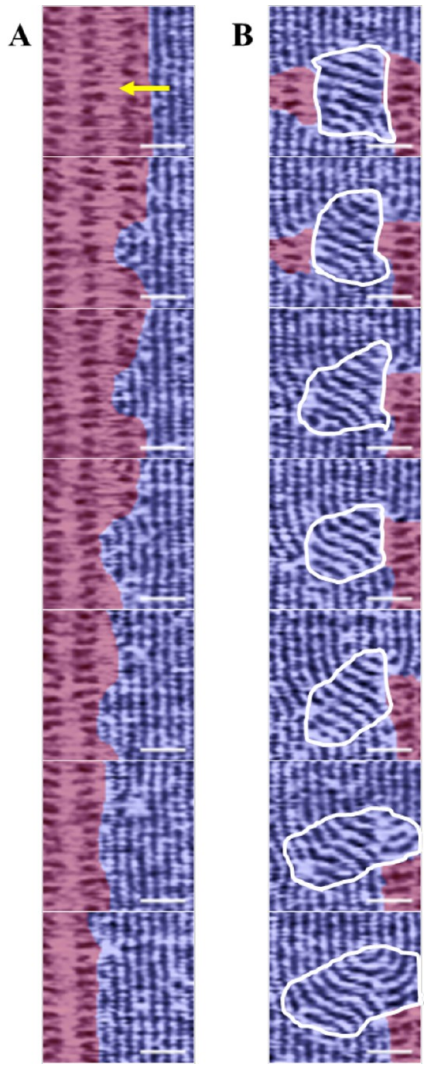

Figure 5. (a) Time series (top-to-bottom with time intervals of 130 s) depicting grain growth during the stitched-to-perpendicular lamellar transition at 210 °C. Stitch domains are highlighted in red. The lamellar grain growth (yellow arrow) progresses orthogonal to the underlying guide pattern and occurs one stitched column at a time. (b) Time series (top-to-bottom with time intervals of 260 s) at 210 °C in the presence of misoriented perpendicular lamellar grains (white bordered regions). When stitches initially connect between columns, misoriented grains form and coarsen that hinder the direct formation of fully aligned patterns.

grain boundaries and defects of opposite orientation and will travel orthogonally across the lamellar pattern, a process known as dislocation glide. An example of dislocation motion is shown in the time series of Figure 6a. Ultimately, the sequential motion of the dislocation across the substrate corrects the misregistry in its wake and produces a well-aligned film, and when two opposite dislocations meet, they will annihilate.

In contrast to previous studies of dislocation mobility on unpatterned substrates, we observed that dislocation motion was not a continuous process.[26] Instead, transits were punctuated by long stationary periods of up to 20 min before rapidly gliding to a new site. Several dislocation trajectories are recorded in Figure 6b. Transit distances were measured to follow multiples of three lamellar periods, distances commensurate with the underlying guide pattern of our 3-fold pattern multiplication samples. When compared with the underlying

DOI: 10.1021/acs.nanolett.7b03881
Nano Lett. 2017, 17, 7717−7723

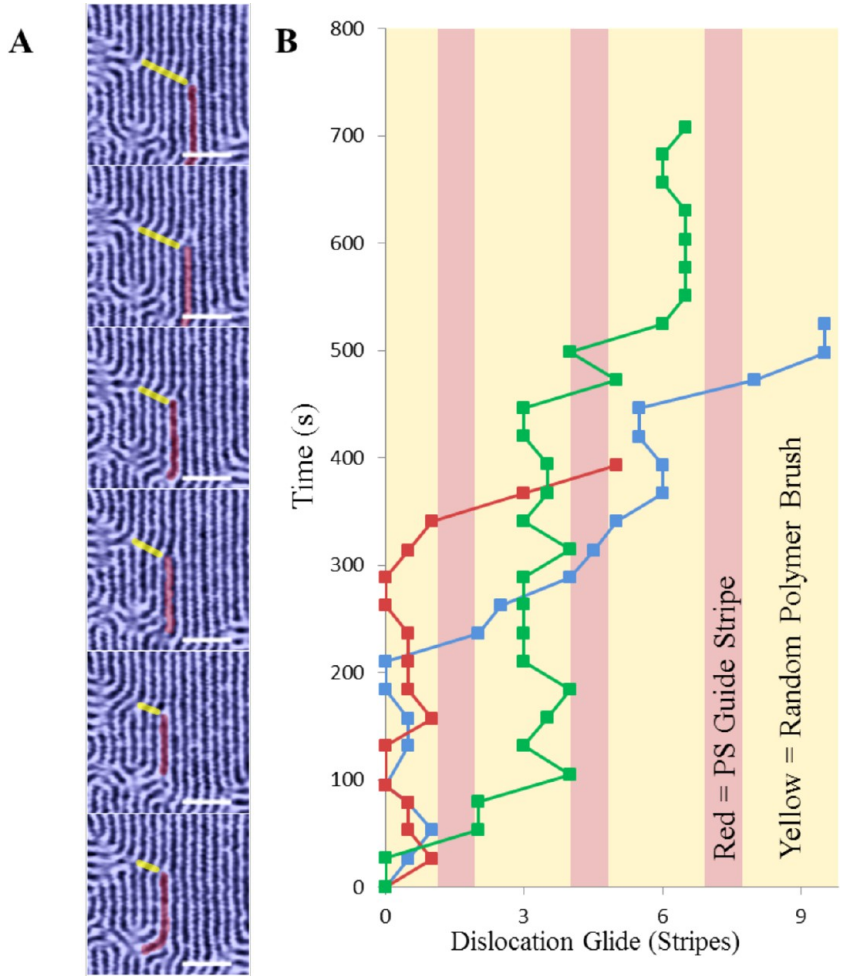

Figure 6. (a) Time series of AFM images at 215 °C showing dislocation glide across six lamellar lines in intervals of 26 s. The dislocation is highlighted in red for clarity. Yellow traces indicate lines of lamellar misregistration. Scale bars are 100 nm. (b) A plot of dislocation trajectories over time at 215 °C for three dislocation glide events in units of lamellar stripes. The blue trace includes the dislocation pictured in (a). Background coloring indicates the locations of the PS guide stripes (red) and the random polymer brush (yellow) in the underlying DSA pattern. Dislocation motion is punctuated, and dislocations are observed to be predominantly trapped over random polymer-brush regions.

guide pattern, stationary dislocations were predominantly found to reside above the centers of nonpreferential brush regions of the guide pattern, indicated by the yellow banded regions in Figure 6b.

For DSA with pattern multiplication, the lamellar stripes above the cross-linked PS regions of the guide pattern are directly aligned by the pattern; the interpolated lamellae are instead indirectly aligned by neighboring lamellar stripes. In this manner, punctuated dislocation mobility reflects the periodic potential energy surface produced by the underlying chemical guide pattern, whereas continuous mobility on graphoepitaxial substrates is governed by the long-range attraction of the opposing dislocation cores. Dislocation residence times varied dramatically, suggesting that the energetics of the trap sites is highly dependent on the local defect structure. However, these observations emphasize the importance of the guide patterning in governing the dynamics of epitaxial alignment.

We have observed the kinetic mechanism for DSA of block copolymers on chemical patterns. Our local AFM measurements provide direct observation of defect ordering mechanisms that are complementary to previous global measurements by GI-SAXS. The chemical pattern hastens alignment to a single-crystal domain and, critically, this process was observed to occur irreversibly. On patterned substrates, ordering followed a single exponential rate law with an apparent energetic barrier of 360 ± 80 kJ/mol from 210−230 °C. Persistent defects were frequently observed to arise as the result of conversion from a metastable stitch morphology, which plays a crucial role in mediating the assembly process. In seeking to prevent defect nucleation, the design of chemical DSA templates must consider not only their role in shaping the final equilibrium state but also their impact on the energetics of these metastable intermediate phases.

Experimental Methods. Chemically patterned substrates were prepared on a TEL Clean Track ACT12 system at IMEC in Leuven, Belgium, following previously reported methods.[32] The template consisted of cross-linked polystyrene (X-PS, AZEMBLY NLD-128) guiding stripes that were preferential for the PS domains and nonpreferential background regions filled with end-grafted PS-*r*-PMMA random copolymers (AZEMBLY NLD-127). The periodic X-PS guiding stripes had a pitch of 84 nm, and each stripe was 8 nm in height and 20 nm in width. The background random copolymer was 6 nm thick, so there was minimal topographic contrast with the guiding stripes.

Unpatterned substrates were coated with a uniform layer of nonpreferential PS-*r*-PMMA polymer brush (AZEMBLY NLD-

DOI: 10.1021/acs.nanolett.7b03881
Nano Lett. 2017, 17, 7717−7723

127) with a thickness of 6 nm. A 35 nm thick layer of lamella-forming PS-*b*-PMMA (AZEMBLY PME-312) was then coated on both types of substrates. This polymer was selected to form structures with 3-fold pattern multiplication on our chosen templates. In situ experiments used samples as cast with no prior annealing. An Asylum Cypher ES AFM was used for in situ real-time imaging while heating the samples at temperatures between 210 and 230 °C with heating rates of 2 °C/s. Samples were allowed to thermally equilibrate for 30 s at temperature before imaging to stabilize thermal drift. Gold-coated Arrow UHF cantilevers were purchased from Nano-World and had resonant frequencies of 1.2−1.6 MHz. Ex situ thermal annealing was performed by heating on a hot plate at 250 °C under nitrogen environment for a series of time intervals and rapidly quenching down to room temperature. Scanning electron microscopy was performed on a Carl Zeiss Merlin SEM.

■ ASSOCIATED CONTENT

Supporting Information

The Supporting Information is available free of charge on the ACS Publications website at DOI: 10.1021/acs.nanolett.7b03881.

AFM movie (312× speed) of thermal annealing and polymer ordering at 210 and 230 °C of PS-*b*-PMMA on a chemical template. (MOV)

■ AUTHOR INFORMATION

Corresponding Author

*E-mail: s-sibener@uchicago.edu. Phone: 773-702-7193.

ORCID

Paul F. Nealey: 0000-0003-3889-142X

S. J. Sibener: 0000-0002-5298-5484

Notes

The authors declare no competing financial interest.

■ ACKNOWLEDGMENTS

This work was supported by the U.S. Department of Commerce, National Institute of Standards and Technology, under award no. 70NHNB14H012 as part of the Center for Hierarchical Materials Design. This was also supported by the NSF-Materials Research Science and Engineering Center at The University of Chicago, grant no. NSF-DMR-14-20709.

■ ABBREVIATIONS

AFM, atomic force microscope
BCP, block copolymer
DSA, directed self-assembly
GI-SAXS, grazing-incidence small-angle X-ray scattering
PMMA, poly(methyl methacrylate)
PS, polystyrene
SEM, scanning electron microscope

■ REFERENCES

(1) Park, C.; Yoon, J.; Thomas, E. L. *Polymer* **2003**, *44* (22), 6725−6760.
(2) Darling, S. B. *Prog. Polym. Sci.* **2007**, *32* (10), 1152−1204.
(3) Kim, H.; Park, S.; Hinsberg, W. D. *Chem. Rev.* **2010**, *110*, 146−177.
(4) Bates, C. M.; Maher, M. J.; Janes, D. W.; Ellison, C. J.; Willson, C. G. *Macromolecules* **2014**, *47*, 2−12.
(5) Angelescu, D. E.; Waller, J. H.; Adamson, D. H.; Deshpande, P.; Chou, S. Y.; Register, R. A.; Chaikin, P. M. *Adv. Mater.* **2004**, *16* (19), 1736−1740.
(6) Amundson, K.; Helfand, E.; Quan, X.; Hudson, S. D.; Smith, S. D. *Macromolecules* **1994**, *27* (22), 6559−6570.
(7) Tong, Q.; Sibener, S. J. *J. Phys. Chem. C* **2014**, *118* (25), 13752−13756.
(8) Ouk Kim, S.; Solak, H. H.; Stoykovich, M. P.; Ferrier, N. J.; de Pablo, J. J.; Nealey, P. F. *Nature* **2003**, *424* (6947), 411−414.
(9) Liu, C.-C.; Ramírez-Hernández, A.; Han, E.; Craig, G. S. W.; Tada, Y.; Yoshida, H.; Kang, H.; Ji, S.; Gopalan, P.; de Pablo, J. J.; Nealey, P. F. *Macromolecules* **2013**, *46* (4), 1415−1424.
(10) Sundrani, D.; Darling, S. B.; Sibener, S. J. *Nano Lett.* **2004**, *4* (2), 273−276.
(11) Ji, S.; Wan, L.; Liu, C.-C.; Nealey, P. F. *Prog. Polym. Sci.* **2016**, *54*, 76−127.
(12) Bita, I.; Yang, J. K. W.; Jung, Y. S.; Ross, C. A.; Thomas, E. L.; Berggren, K. K. *Science* **2008**, *321* (5891), 939−943.
(13) Hur, S.-M.; Thapar, V.; Ramírez-Hernández, A.; Khaira, G.; Segal-Peretz, T.; Rincon-Delgadillo, P. A.; Li, W.; Müller, M.; Nealey, P. F.; de Pablo, J. J. *Proc. Natl. Acad. Sci. U. S. A.* **2015**, *112* (46), 14144−14149.
(14) Li, W.; Nealey, P. F.; de Pablo, J. J.; Müller, M. *Phys. Rev. Lett.* **2014**, *113* (16), 168301.
(15) Li, W.; Müller, M. *Macromolecules* **2016**, *49*, 6126−6138.
(16) Li, W.; Müller, M. *Annu. Rev. Chem. Biomol. Eng.* **2015**, *6* (1), 187−216.
(17) Paik, M. Y.; Bosworth, J. K.; Smilges, D.-M.; Schwartz, E. L.; Andre, X.; Ober, C. K. *Macromolecules* **2010**, *43* (9), 4253−4260.
(18) Gu, X.; Gunkel, I.; Hexemer, A.; Gu, W.; Russell, T. P. *Adv. Mater.* **2014**, *26* (2), 273−281.
(19) Harrison, C.; Adamson, D. H.; Cheng, Z.; Sebastian, J. M.; Sethuraman, S.; Huse, D. A.; Register, R. A.; Chaikin, P. M. *Science* **2000**, *290* (5496), 1558−1560.
(20) Welander, A. M.; Kang, H.; Stuen, K. O.; Solak, H. H.; Müller, M.; de Pablo, J. J.; Nealey, P. F. *Macromolecules* **2008**, *41* (8), 2759−2761.
(21) Ruiz, R.; Bosworth, J. K.; Black, C. T. *Phys. Rev. B: Condens. Matter Mater. Phys.* **2008**, *77* (5), 54204.
(22) Edwards, E. W.; Stoykovich, M. P.; Müller, M.; Solak, H. H.; de Pablo, J. J.; Nealey, P. F. *J. Polym. Sci., Part B: Polym. Phys.* **2005**, *43* (23), 3444−3459.
(23) Yufa, N. A.; Li, J.; Sibener, S. J. *Polymer* **2009**, *50*, 2630−2634.
(24) Ryu, H. J.; Tong, Q.; Sibener, S. J. *J. Phys. Chem. Lett.* **2013**, *4* (17), 2890−2895.
(25) Tong, Q.; Zheng, Q.; Sibener, S. J. *Macromolecules* **2014**, *47* (13), 4236−4242.
(26) Tong, Q.; Sibener, S. J. *Macromolecules* **2013**, *46* (21), 8538−8544.
(27) Segal-Peretz, T.; Ren, J.; Xiong, S.; Khaira, G.; Bowen, A.; Ocola, L. E.l; Divan, R.; Doxastakis, M.l; Ferrier, N. J.; de Pablo, J. J.; Nealey, P. F. *ACS Nano* **2017**, *11*, 1307−1319.
(28) Rahman, A.; Majewski, P. W.; Doerk, G.; Black, C. T.; Yager, K. G. *Nat. Commun.* **2016**, *7*, 13988.
(29) Mansky, P.; Russell, T. P.; Hawker, C. J.; Mays, J.; Cook, D. C.; Satija, S. K. *Phys. Rev. Lett.* **1997**, *79* (2), 237−240.
(30) Mansky, P.; Liu, Y.; Huang, E.; Russell, T. P.; Hawker, C. *Science* **1997**, *275* (5305), 1458−1460.
(31) Segal-Peretz, T.; Winterstein, J.; Doxastakis, M.; Ramírez-Hernández, A.; Biswas, M.; Ren, J.; Suh, H. S.; Darling, S. B.; Liddle, J. A.; Elam, J. W.; de Pablo, J. J.; Zaluzec, N. J.; Nealey, P. F. *ACS Nano* **2015**, *9* (5), 5333−5347.
(32) Rincon Delgadillo, P. A.; Gronheid, R.; Thode, C. J.; Wu, H.; Cao, Y.; Somervell, M.; Nafus, K.; Nealey, P. F. All Track Directed Self-Assembly of Block Copolymers: Process Flow and Origin of Defects. In *Alternative Lithographic Technologies IV*; Tong, W. M., Ed.; SPIE: Bellingham, WA, 2012.

DOI: 10.1021/acs.nanolett.7b03881
Nano Lett. 2017, 17, 7717−7723